Regular Article

Numerical simulation and scaling of droplet deformation in a hyperbolic flow[*]

Erfan Kadivar[1,a] and Atefeh Alizadeh[2]

[1] Department of Physics, Shiraz University of Technology, Shiraz, 71555-313, Iran
[2] Department of Physics, Faculty of Sciences, Persian Gulf University, 75168 Bushehr, Iran

Abstract. Motivated by a recent experiment (C. Ulloa *et al.*, Phys. Rev. E **89**, 033004 (2014)), droplet deformation in a flat microfluidic channel having a cross intersection with two inlet channels and two outlet channels, *i.e.* hyperbolic flow, is numerically investigated. Employing the boundary element method (BEM), we numerically solve the Darcy equation in the two dimensions and investigate droplet motion and droplet deformation as the droplet enters the cross intersection. We numerically find that the maximum deformation of droplet depends on droplet size, capillary number, viscosity ratio and flow rate ratio of the two inlets. Our numerical scaling is in good agreement with the experimental scaling report.

1 Introduction

Microfluidics is a multidisciplinary field with a wide variety of applications in physics, biomedical, chemical biology, oil industry and so on. Microfluidics is a field of fluid dynamics which deals with the manipulation and control of fluids in devices which have characteristic lengths in the micrometer range. Indeed, the behavior of liquids in the micro range greatly differs from the one in the macro domain. Factors such as viscosity and surface tension are playing an important role in microfluidics. One way to study the behavior of liquid-liquid interface is to investigate droplet motion in microfluidic channels [1–4]. A large number of studies have been carried out on droplet motion in microchannels [5–9], as well as phenomena like breakup [10,11], droplet coalescence [12–14], and droplet deformation.

Droplet deformation in a flow field constitutes an interesting field in the soft matter field. So far, droplet deformation has been studied widely experimentally and numerically in the literature. The first classical study of droplet deformation has been reported by Taylor who studied an isolated droplet in a simple shear flow field when the droplet is located far enough from the channel walls [15,16]. Rallison studied the deformation of small viscous droplets and bubbles in a shear flow field [17]. Droplet deformation in the presence of a two-dimensional

linear flow field has been experimentally investigated by Bentley and Leal [18].

Recently, Brosseau *et al.* investigated the influence of droplet confinement on its deformation, in a sudden expansion geometry. They have seen that droplet deformation in a microchannel strongly depends on droplet confinement in the channel before a sudden expansion region. They have shown that in the geometry of a planar sudden expansion, the droplet maximum deformation follows two regimes linked to its confinement in the microfluidic channel [19]. They also investigated the influence and adsorption of surfactants by following the idea of a microfluidic tensiometer. In a recent work, Ulloa *et al.* experimentally studied droplet deformation in a diverging flow at low Reynolds numbers and large aspect ratio of droplet radius to channel height [20].

A series of numerical studies have been carried out to investigate droplet deformation by using different numerical methods. The effect of the surfactant-laden interface on the droplet deformation in an extensional flow has been numerically studied by Eggleton and Stebe [21]. Their numerical results indicate that the behavior of droplet deformation is strongly influenced both by surfactant mass transfer rate and concentration of surfactant present. Xi and Duncan used a three-dimensional Lattice Boltzmann model to simulate the droplet deformation in a straight channel. They have also simulated the effect of larger shear rates and have successfully evolved the sheared single droplet to breakup [22]. Nagel and Gallaire numerically investigated the droplet dynamics by using the two-dimensional Darcy-Brinkman equation model [23].

Stan *et al.* have experimentally and numerically investigated hydrodynamic lift forces acting on drops and

---

bubbles in microchannels [24,25]. Their results indicate that droplets and bubbles can be reproducibly positioned and centered in microfluidic channels without using sheath fluids. The evolution of the droplet deformations with the lateral positions in a straight microfluidic channel has been studied by Chen *et al.* [26]. They have investigated the effect of droplet size, capillary number, viscosity ratio, and lateral position on the droplet deformation and droplet migration.

The present study is motivated by the recent experimental work of Ulloa *et al.* on droplet deformation [20]. In this work, we study the deformation of a droplet flowing through a microfluidic channel having a cross-intersection with two inlet channels and two outlet channels making an angle of 90° relative to each other. We focus our attention on the high aspect ratio of channel width to channel height. In this limit, the fluidic resistance in the microfluidic channel is high. Experimental observations indicate that the velocity profile in a thin channel and in the direction of channel thickness is assumed to be parabolic, but far from walls it is almost constant along the channel width. Therefore, a two-dimensional flow which is constant far from walls and in the channel width direction can be governed by the Darcy equation. The droplet deformation has been numerically calculated as a function of droplet size, surface tension, viscosity ratio, and flow rate ratio.

This paper is structured as follows: In the following section 2, we will formulate the Darcy equation and boundary conditions for the pressure and velocity field for a quasi-two-dimensional droplet in a flat microfluidic channel having a junction with two inlet channels and two outlet channels. The numerical procedure to solve the integral equation for pressure field as well as for local droplet velocity are also contained in sect. 2. The results of our numerical solutions, including the dependence of the maximum deformation on the droplet size, capillary number, and flow rate ratio are reported in sect. 3. Finally, in sect. 4 we summarize our findings, conclude, and give an outlook on possible future work in this field.

2 Physical model and numerical methods

In this work, we will numerically compute the deformation of a monodisperse emulsion droplet flowing in a flat microfluidic channel having a cross-intersection with two inlet channels and two outlet channels making an angle of 90° relative to each other. The width of inlets, outlets, and cross-section is equal to W. The inlet channels are along the x-axis and the outlet channels are along the y-axis (see fig. 1). We consider flow past a two-dimensional droplet containing a droplet phase labeled d, and suspended in a continuous phase labeled c. Continuous phase viscosity is μ_c and viscosity of droplet phase is $\lambda\mu_c$, where $\lambda(\lambda < 1)$ is the viscosity ratio. In the Hele-Shaw limit which refers to the case that channel height, H, is assumed to be much smaller than droplet radius, the droplet will be confined between the top and bottom walls of the microfluidic channel. In addition to vertical confinement, the droplet will be deformed by the incident flows.
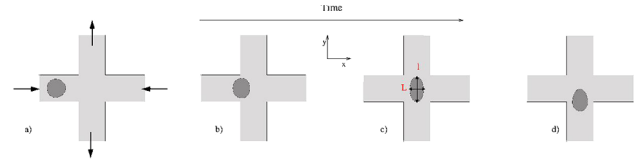
Fig. 1. Snapshots of a droplet deformation in the flat microfluidic channel at different times. Black arrows in (a) indicate the incoming and outcoming flow directions. Numerical parameters are $Ca = 0.02$, $\Lambda = 1$, $\mu = 0.008$ and $a_d = 22.7$.

Due to the small length scale, the flow resistance in the microchannels is high. Therefore, flow rates usually range between a few nl/min to μl/min and the Reynolds number is small. Experimental observations indicate that at a thin channel, the velocity profile in the direction of channel height, z-axis, is assumed to be parabolic. However, far from the walls, the velocity profile is almost constant along the y-axis. It is easy to verify that by increasing the aspect ratio of channel width to channel height, the velocity field computed from the 3D Stokes equation in the x-y plane and far from the walls tends to a constant value in the y-direction. Therefore, instead of solving the 3D Stokes equation, we solve a depth-averaged problem which is labeled two-dimensional problem. It is important to note that it has been shown that even in the complex thermocapillary flow around a droplet, the averaged model agrees perfectly with the 3D Stokes' one [27]. Hence, This flow can be well approximated by a two-dimensional description. Such two-dimensional flow in a Hele-Shaw cell obeys Darcy's law; this laminar flow is mathematically equivalent to a flow in a porous medium [28,29].

In the Hele-Shaw limit, the flow velocities obey locally a Poiseuille profile

$$\boldsymbol{v}(x,y,z) = h(z)(\bar{v}_x, \bar{v}_y, 0), \tag{1}$$

where $h(z) = 3/2(1 - 4z^2/H^2)$ and $\bar{\boldsymbol{v}}$ indicates the depth-averaged velocity. Deviations from the Poiseuille profile become apparent once the distance to the side walls becomes the order of cell height, H, or smaller. On a small length scale of H, the depth-averaged velocity $\boldsymbol{v}(x,y,z) = (\bar{v}_x, \bar{v}_y)$ for both droplet and continuous phase are used in this work. Under this assumption, when the gravitational force is negligible, the velocity field inside and outside of droplets are governed by the continuity equation

$$\bar{\boldsymbol{v}}_i = -\frac{H^2}{12\mu_i}\boldsymbol{\nabla}p_i \quad \text{on } \Omega_i \quad \text{with } i \in \{c, d\}, \tag{2}$$

$$\boldsymbol{\nabla} \cdot \bar{\boldsymbol{v}}_i = 0 \quad \text{on } \Omega_i \quad \text{with } i \in \{c, d\}, \tag{3}$$

respectively. $\boldsymbol{\nabla} = (\partial_x, \partial_y)$ is the two-dimensional Nabla operator, $p(x,y)$ is the pressure, μ is the viscosity, and $\bar{\boldsymbol{v}}$ is the depth-averaged velocity. We denote $2D$ vectors in the central plane of the channel by boldface symbols.

Droplet interface conditions are continuity of velocity and discontinuity of interface stresses. The evolution of the droplet interface is governed by mass conservation. If there is no mass transfer through the interface, the kinematic

condition is satisfied at the droplet-continuous phase interface by using the continuity of the normal velocity component. This boundary condition reads

$$\mathbf{n}_\mathrm{d} \cdot \bar{\boldsymbol{v}}_\mathrm{c} = \mathbf{n}_\mathrm{d} \cdot \bar{\boldsymbol{v}}_\mathrm{d} \neq 0 \quad \text{on } \Gamma_\mathrm{cd}, \tag{4}$$

where the unit normal vector, $\mathbf{n}_\mathrm{d}$, points from the interior of the droplet phase into the continuous phase at droplet interface and Γ_cd is the two-dimensional droplet contour. It is important to emphasise, in the case, that the interface is independent of time, meaning that the interface is not translating relative to the origin of the coordinate system, and the normal component of velocity at fluid-fluid interface will be zero.

On the liquid-liquid interface, the stress boundary condition due to surface tension contains a jump in normal stress, due to the curvature, and in tangential stresses, due to the varying surface tension which is called Marangoni effect. The jump condition on the stress, at a fluid-fluid interface, can be written as

$$\mathbf{n}_\mathrm{d} \cdot (\mathbf{T}_\mathrm{c} - \mathbf{T}_\mathrm{d}) = \frac{\pi}{4} \gamma K \mathbf{n}_\mathrm{d} - \boldsymbol{\nabla}_s \gamma, \tag{5}$$

where $\mathbf{T}$ is interface stresses tensor, γ is surface tension, $\mathbf{n}_\mathrm{d}$ is the unit normal vector at droplet interface and K is the local curvature. In the absence of Marangoni stresses, and in the Hele-Shaw limit, which is valid asymptotically in the slow flow limit, the pressure inside, p_d, and outside of droplet, p_c, is discontinuous due to surface tension, γ and local curvature, K. This boundary condition reads

$$p_\mathrm{c} - p_\mathrm{d} = \frac{\pi}{4} \gamma K, \tag{6}$$

where the prefactor $\pi/4$ is related to the real droplet microfluidic system in which a non-wetting condition at the top and bottom wall of the Hele-Shaw cell is assumed [30].

The boundary conditions require that the velocity must vanish over all channel walls, Γ_w. We have

$$\mathbf{n}_\mathrm{w} \cdot \boldsymbol{\nabla} p_\mathrm{c} = 0 \quad \text{on } \Gamma_\mathrm{w}, \tag{7}$$

where the normal vector $\mathbf{n}_\mathrm{w}$ on Γ_w points from the inside of the wall into the continuous phase. At the open ends, *i.e.*, at the inlets and outlets of the microfluidic channel, we assume that the flow velocity of the continuous phase is constant. In this case the boundary condition at the open ends reads

$$-\alpha_\mathrm{c} \mathbf{n}_\mathrm{w} \cdot \boldsymbol{\nabla} p_\mathrm{c} = \begin{cases} v_\mathrm{in} & \text{inlet} \\ v_\mathrm{out} & \text{outlets} \end{cases} \quad \text{on } \Gamma_\mathrm{o}, \tag{8}$$

where $\alpha_\mathrm{c} = \frac{H^2}{12\mu_\mathrm{c}}$ is the mobility of the continuous phase, Γ_o is a straight line cutting through the open ends of the microfluidic channel and v_in and v_out are the constant normal velocities of the continuous phase at the inlets and outlets of the channel, respectively (see fig. 1).

Employing the continuity equation $\boldsymbol{\nabla} \cdot \bar{\mathbf{v}} = 0$, the pressure in the dispersed and the continuous phases satisfy the Laplace equation

$$\nabla^2 p_i = 0, \quad i \in \{\mathrm{d}, \mathrm{c}\}. \tag{9}$$

Solutions to eq. (9) for appropriate boundary conditions (eqs. (4), (6), (7), (8)), together with the Darcy equation (2) describe the pressure and velocity fields of the liquid in the droplet phase, (d), and continuous phase, (c).

2.1 Numerical methods

In order to numerically evolve the droplet interface under flowing in time, the local depth-averaged velocity components, v_x and v_y, at the droplet contour have to be calculated. One way to obtain the relevant boundary data of the velocity field is to numerically compute a self-consistent integral equation for pressure field p_c of the continuous phase on the boundaries $\Gamma_\mathrm{cd} \cap \Gamma_\mathrm{w}$ to its normal derivative $\nabla_\mathrm{n} p_\mathrm{c}$. Following the formulation of Pozrikidis [31], the pressure field of the continuous phase satisfies a self-consistent integral equation of the following form

$$p_\mathrm{c}(\mathbf{r}_0) = \int_{\Gamma_\mathrm{w}, \Gamma_\mathrm{o}} p_\mathrm{c} \mathbf{n}_\mathrm{w} \cdot \boldsymbol{\nabla} \mathcal{G}(\mathbf{r}, \mathbf{r}_0) \mathrm{d}\ell - \int_{\Gamma_\mathrm{o}} \mathcal{G}(\mathbf{r}, \mathbf{r}_0) \mathbf{n}_\mathrm{w} \cdot \boldsymbol{\nabla} p_\mathrm{c} \mathrm{d}\ell$$

$$- \int_{\Gamma_\mathrm{cd}} \left\{ \frac{\pi}{4} \alpha \gamma K \mathbf{n}_\mathrm{d} \cdot \boldsymbol{\nabla} \mathcal{G}(\mathbf{r}, \mathbf{r}_0) - (1 - \alpha) p_\mathrm{c} \mathbf{n}_\mathrm{d} \cdot \boldsymbol{\nabla} \mathcal{G}(\mathbf{r}, \mathbf{r}_0) \right\} \mathrm{d}\ell, \tag{10}$$

where α is the mobility ratio of the droplet to continuous phase ($\alpha = 1/\lambda = \mu_\mathrm{c}/\mu_\mathrm{d}$), and $\mathbf{r}_0$ is a point on the boundary $\Gamma_\mathrm{cd} \cap \Gamma_\mathrm{w} \cap \Gamma_\mathrm{o}$ of the continuous phase. The function

$$\mathcal{G}(\mathbf{r}, \mathbf{r}_0) = -\frac{1}{2\pi} \ln |\mathbf{r} - \mathbf{r}_0| \tag{11}$$

represents the free Green's function of the two-dimensional Laplace equation eq. (9), where $\mathbf{r} = (x, y)$ and $\mathbf{r}_0 = (x_0, y_0)$ are the field and the singular points, respectively.

Before numerically solving the self-consistent integral equation, it is useful to define four basic parameters which are needed to express all physical quantities in this work. In this way we select the length scale $L_0 \equiv H$, the time scale $T_0 \equiv \mu_\mathrm{c} H/\gamma$, the pressure scale $p_0 \equiv \gamma/H$, and the capillary number $Ca = \mu_\mathrm{c} v_\mathrm{in}/\gamma$. The dimensionless droplet area, a_d, is defined as the droplet area divided by the squared channel height, $a_\mathrm{d} = \pi R^2/H^2$. Here, and in the remainder of this article, we will denote all non-dimensional rescaled lengths and physical quantities by lower case symbols.

2.2 Boundary element discretization

In order to numerically solve the self-consistent integral equation, the droplet-continuous phase interface and channel walls have to be discretized into a collection of one-dimensional boundary elements [31]. We discretized the droplet-continuous phase interface by using the cubic-spline method. This method provides us a globally smooth slope and curvature at the end point of elements. In this way, we described the droplet boundary with N nodes.

The coordinates of each element are expressed in parametric form by the cubic polynomial. Because the droplet is a closed surface, we used the periodic cubic-spline in which periodicity conditions for the first and second derivative at the first and last nodes are imposed. In contrast to the droplet contours, fixed boundaries like walls and inflow and outflow boundaries are discretized by straight segments. The mesh independence has been verified by calculating the droplet area as a function of time. According to the continuity equation, it is clear that the droplet area must be constant over time. It was found that 138 points for droplet contour and 400 straight elements for fixed boundaries are satisfactory and any increase beyond this mesh size would lead to insignificant changes in results.

The boundary integral equation is discretized with a collection method and integrated by a *Gauss-Legendre* quadrature with 12 nodes. Therefore, we calculate the pressure and velocity at the collection points. After that, we update the position of the points by using an explicit Euler method and Runge-Kutta method. Using the explicit Euler method the interface droplet is advanced in discrete time steps:

$$x^{(n+1)} = \int_{t=n}^{t=n+1} \bar{v}_x \mathrm{d}t + x^{(n)},$$

$$y^{(n+1)} = \int_{t=n}^{t=n+1} \bar{v}_y \mathrm{d}t + y^{(n)}, \qquad (12)$$

where $\bar{\boldsymbol{v}}$ is the velocity field obtained by solving the boundary element problem at node $\mathbf{r}^{(n)}$. Since relative positions of the points on Γ_{cd} are changed over time, it is necessary to remesh the splines at each time step. This remeshing is calculated by cubic interpolation to compute new points on the droplet contour [8]. Since the boundary element method is only implemented for boundaries which are discretized, it is unnecessary to remesh the whole domain as the interface evolves.

3 Results

Motivated by a recent experiment [20], we present the study of droplet deformation flowing through a flat microfluidic channel. As already mentioned in the physical model section (sect. 2), our considered channel geometry consists of straight channel having a cross-shaped intersection with two inlet channels and two outlet channels which make an angle of 90° relative to each other (see fig. 1). All channels in the network are characterized by a uniform width W. The channel length is fixed by 20 times the channel width. The ratio of channel width to channel height is approximately 8. The continuous fluid is injected from two opposite sides into the inlet channels. The flux ratio is characterized by the dimensionless parameters $\Lambda = Q_R/Q_L \geq 1$, where Q_L, Q_R are the flow rates of the left-flow and right-flow inlets, respectively. In all numerical simulations, we control the outlet fluxes by the total flow rate, $Q = Q_R + Q_L$, at the outlets of the microfluidic
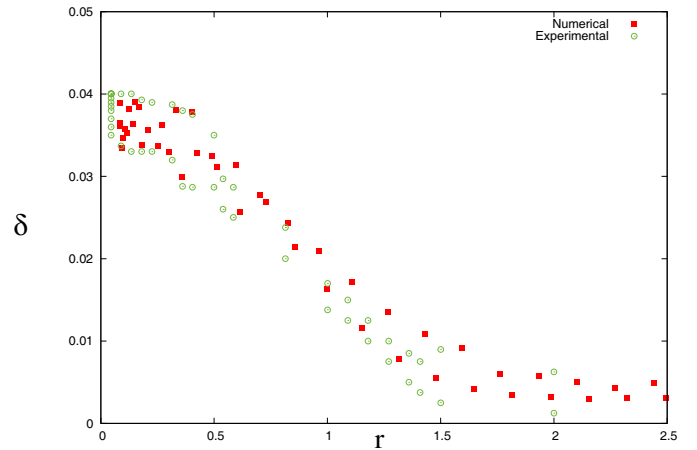

Fig. 2. Droplet deformation profile, $\delta(x)$, against droplet position, r, at capillary number $Ca = 0.008$, viscosity ratio $\mu = 0.008$. Green open circles are extracted from the experimental data [20] and red squares correspond to our simulations. Control parameters are $a_{\mathrm{d}} = 1.85$, and $\Lambda = 1$.

channel. From the left inlet channel, the droplet enters the cross-shaped section. When a deformable droplet approaches the cross section the droplet decelerates and deforms. Eventually, the droplet leaves the stagnation point and flows through one of the exits. Figure 1 illustrates the snapshots of a droplet that enters the cross-section from the left at several times. As one can see in fig. 1, the droplet deformation is calculated by the ratio $\delta = (l - L)/(l + L)$, where L is the axis of the droplet in the x-direction and l its axis in the y-direction. The deformation of the droplet is computed as a function of its dimensionless distance from the center of the cross-intersection, $r = \sqrt{x^2 + y^2}$.

To validate the consistency of the numerical model, we compare the droplet deformation profile reported by Ulloa *et al.*'s experimental observations [20] to the simulated ones which were obtained using the same conditions of capillary number, and droplet size. Simulation and experiment results seem to be in good quantitative agreement, as shown in fig. 2.

Figure 3 shows a typical evolution curve of δ as a function of distance from the center of the cross-intersection, r, and dimensionless travel time, t. The red line shows the evolution of δ when the droplet flows into the cross-intersection while the green line is used for droplets leaving it. As one can see in fig. 3, the droplet deformation increases monotonically as the droplet approaches the stagnation point and deformation reaches its maximum value. However, the droplet deformation backs into a circular shape as it flows into the outlet channel (see the movie given as Supplementary Material). The curves of droplet deformation when droplet flows into and out of the cross-intersection differ. This is due to the effect of the continuous flow on the droplet deformation in the presence of a hyperbolic flow. When a droplet flows into the cross-intersection, a diverging external flow is experienced by droplet, while a droplet flowing out of the cross-section experiences a convergent flow. The difference between the
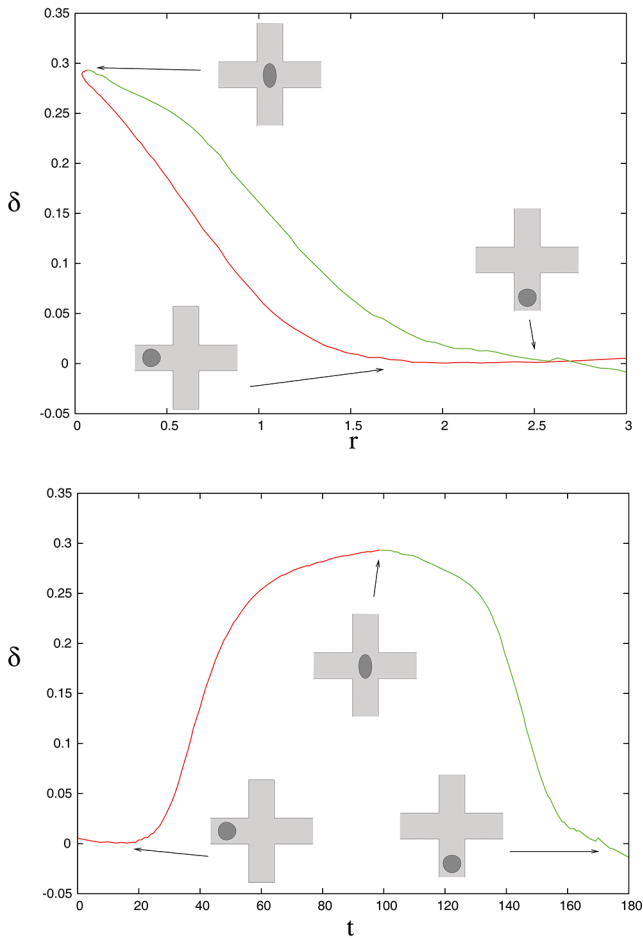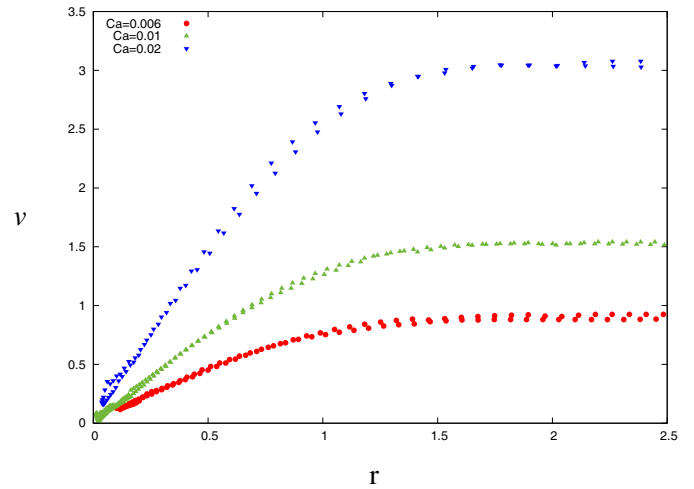
Fig. 3. Droplet deformation flowing through a microchannel. δ is plotted as a function of the dimensionless distance between the droplet and the center of the cross-intersection (top panel) and of the dimensionless time when the droplet flows into (red line) and out of (green line) the cross-intersection (bottom panel). Numerical parameters are $Ca = 0.02$, $\Lambda = 1$, $a_{\rm d} = 22.7$, $\mu = 0.008$.
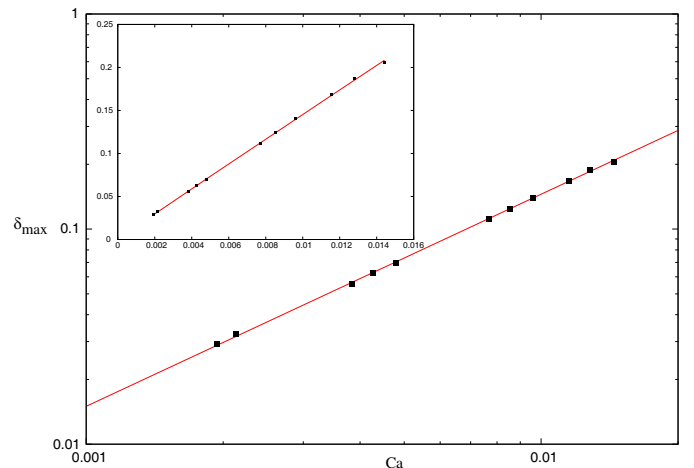
Fig. 4. Droplet speed profile v as a function of dimensionless distance between the droplet center and the center of the cross-intersection, $r = 0$, for different values of the capillary number. Numerical parameters are $a_{\rm d} = 22.7$, $\mu = 0.008$, $\Lambda = 1$, and $Ca = 0.02$.

Fig. 5. Dependence of the maximum deformation of the droplet on the capillary number for a given value of droplet size, $R/H = 2.7$. The inset shows a non-logarithmic plot. Flow rate ratio $\Lambda = 1$.

two graphs increases by increasing the capillary number (see figs. 2 and 3 (top)). This behavior is due to the effect of the capillary number on the convergence of the hyperbolic flow. This behavior indicates that the flow in the presence of a droplet is an irreversible phenomenon.

The dependence of the droplet maximum deformation upon the capillary number is obtained by varying the surface tension, and continuous phase velocity. To investigate the variation of the droplet speed with droplet position, we compute the instantaneous velocity by a division of the difference in the position of the droplet center between two successive positions by the step-time. Figure 4 illustrates the droplet speed as a function of droplet position for different capillary number. The droplet speed monotonically decreases as the droplet enters the cross-intersection and its speed reaches a minimum value. However, the droplet speed monotonically increases as it flows into the outlet channel.

In order to quantify the dependence of the maximum deformation, $\delta_{\max}$, on the droplet size and capillary num-

ber, we fix the droplet size and vary the surface tension and flow rate, *e.g.* the capillary number. The effect of increasing the capillary number on the droplet is to elongate the droplet as it enters the intersection. It is important to emphasise that the numerical parameters such as viscosity ratio, flow rate, and surface tension are chosen such that the channel network operates in a dynamic regime of the capillary number where the droplet deforms but does not breakup when passing through the cross-intersection. For given values of droplet size and viscosity ratio, the critical capillary number, $Ca_{\rm c}$ for droplet breakup is reported in the literature [10,11].

Figure 5 presents the maximum droplet deformation as a function of capillary number for given values of the dimensionless droplet size and viscosity ratio. It is found that the maximum droplet deformation varies linearly
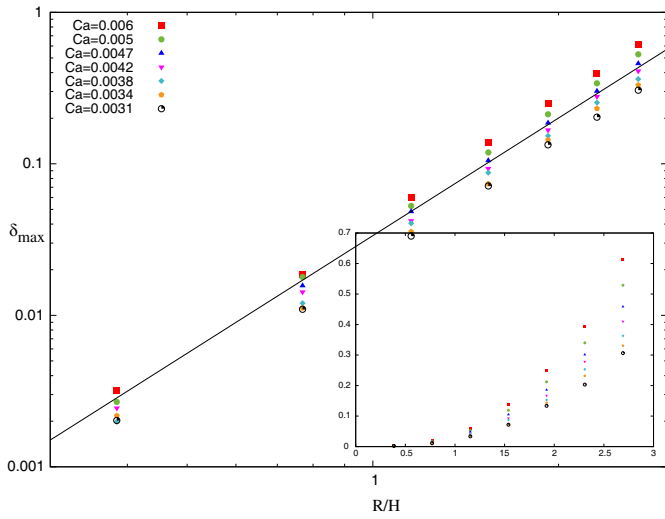
Fig. 6. Dependence of the maximum deformation of the droplet on its size. Symbols are related to different surface tensions. The inset illustrates a non-logarithmic plot. Flow rate ratio $\Lambda = 1$.
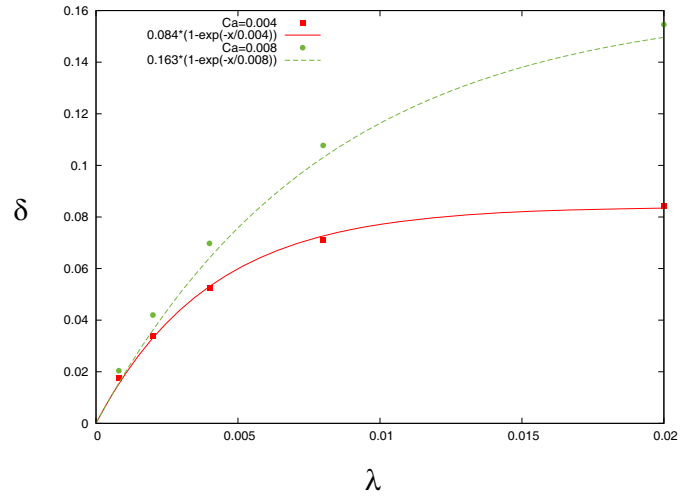

Fig. 7. The maximum deformation of a droplet as a function of the viscosity ratio for a given value of the droplet size, $a_{\rm d} = 22.7$. Solid squares and circles are related to $Ca = 0.004$ and $Ca = 0.008$, respectively. The solid and dashed lines are the best numerical fitting results.

with the capillary number (varies with the inverse of the surface tension). Our numerical results indicate that for a two-dimensional model, the exponent is 1.01 which is very close to one. This numerical scaling is in good agreement with the theoretical model in the small-deformation limit [15,16,20]. The exponent on the capillary number may vary in the three-dimensional channels or large-deformation regime [32,33].

Similarly, the maximum droplet deformation as a function of the droplet size for different values of the capillary number is illustrated in fig. 6. It is observed that the maximum droplet deformation increases by increasing the droplet size, $a_{\rm d}$. The capillary number and droplet size dependence of the maximum droplet deformation are plotted on a log-log scale in figs. 5 and 6. The maximum droplet deformation can be rescaled according to the capillary number, Ca, and the non-dimensional droplet radius, R/H, in the following way:

$$\delta_{\max} \propto (R/H)^{2.58} Ca^{1.01}. \tag{13}$$

It is to be noted that a power law $Ca^{0.91}$ and $R^{2.59}$ were experimentally found by Ulloa *et al.* [20] in their description of the elongation of a viscous droplet in microfluidic channel. Our numerical scaling is in good agreement with the experimental results [20].

We investigate the influence of the viscosity ratio, λ, on the droplet deformation while we hold the other parameters constant. To change the value of the viscosity ratio without affecting the capillary number, we keep the viscosity of the continuous phase and change the droplet viscosity. Our numerical results indicate a nonlinear relation between the viscous ratio and droplet deformation. The droplet deformation increases by increasing the viscosity ratio. A plateau region in the maximum deformation curve appears as the viscosity ratio increases. Figure 7 illustrates the maximum droplet deformation as a function

of viscosity ratio for two given values of the capillary number. The dots in fig. 7 are numerical data, the solid and dashed lines are the best numerical fitting results. Therefore, the maximum droplet deformation depends on the viscosity ratio as

$$\delta_{\max} \propto (1 - \exp(-b\lambda)), \tag{14}$$

where b is constant parameter. Our numerical results are in good agreement with the experimental observation that the droplet deformation exponentially increases by increasing the viscosity ratio [24,26].

We can now identify another characteristic of a droplet deformation by invoking the rescaling of $\delta_{\max}$ with Λ which has been not experimentally investigated in ref. [20]. The position of stagnation point, maximum deformation of the droplet and the droplet shape at maximum deformation depend on the flow rate ratio of two inlets of the microchannel, $\Lambda = Q_R/Q_L$. In order to investigate the dependence of the droplet deformation on the flow rate ratio, the left flow rate is kept to be constant and the right flow rate varies. We show in fig. 8 the droplet contour for a set of flow rate ratio at a given value of droplet size and capillary number. These profiles show that the position of stagnation point shifts toward the inlet channel having low flow rate. The position deviation, Δr, between the position of the stagnation point, r, and the center of cross-intersection, as function of flow rate ratio of two inlets is plotted in fig. 9. The deviation gradually increases to reach a plateau form which is restricted by cross-intersection length.

To study the effect of the flow rate ratio on the maximum droplet deformation, we keep the capillary number, viscosity ratio and droplet size constant and vary the flow rate ratio. The maximum droplet deformation $\delta_{\max}$ is calculated for given values of droplet size and capillary number. The maximum deformation $\delta_{\max}$ as a function of Λ
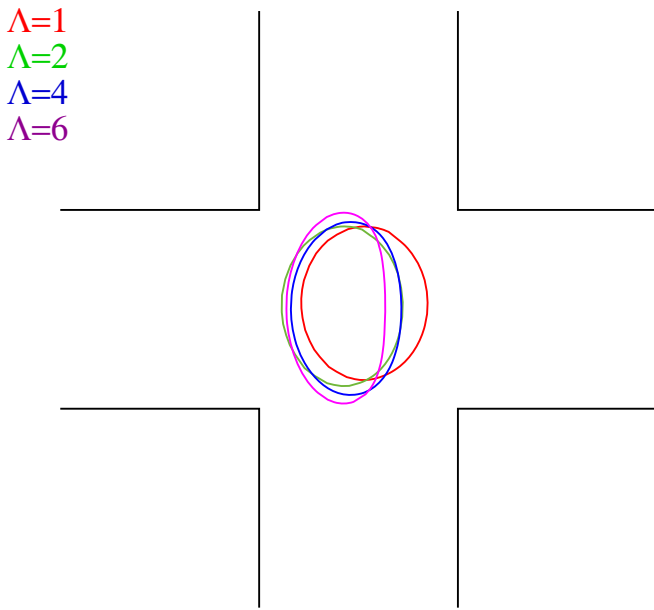
Fig. 8. Simulated droplet contour, and position at its maximum deformation for different values of the flow rate ratio of two inlets at a given value of droplet size. The left flow rate is kept constant.
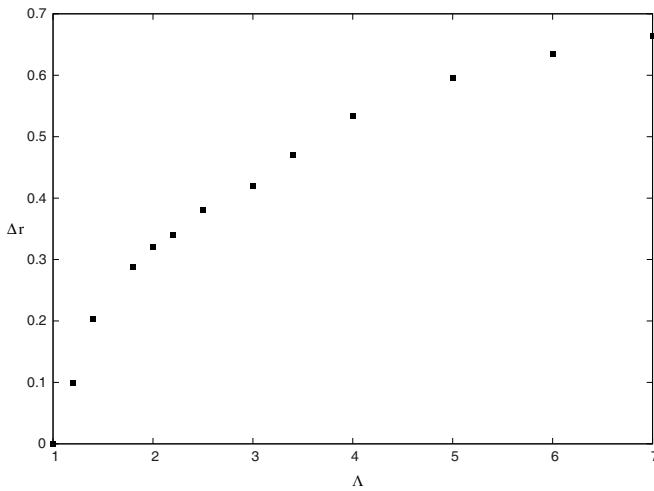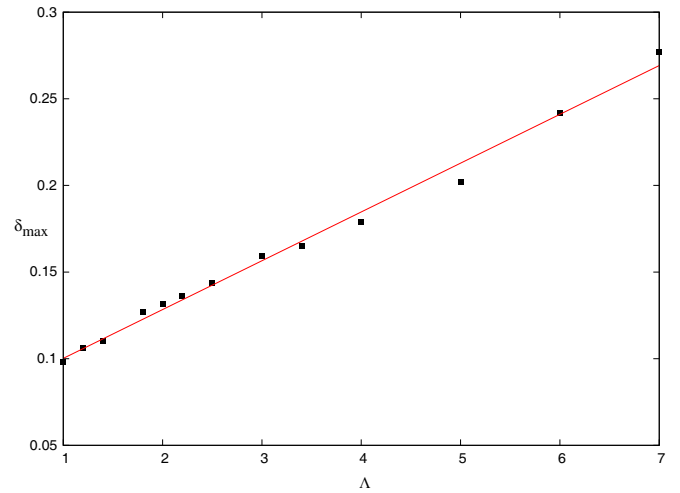

Fig. 9. The stagnation point deviation of the maximum deformation as a function of the flow rate ratio of two inlets for a given value of droplet size and surface tension.

is shown in fig. 10. Numerical simulation shows a dependence in $\Lambda^{1.02}$.

To summarize our numerical findings, the maximum droplet deformation can be rescaled according to the capillary number, Ca, non-dimensionless droplet radius, R/H, viscosity ratio in the following way:

$$\delta_{\max} \propto (1 - \exp(-b\lambda))(R/H)^{2.58}Ca^{1.01}\Lambda^{1.02}. \quad (15)$$

This numerical scaling is in good agreement with the theoretical and experimental results in the confined microfluidic channel [15,20,24].

Fig. 10. The maximum deformation as a function of flow rate ratio of two inlets for a given value of droplet size and surface tension. The left flow rate is kept constant.

4 Conclusion

By employing the boundary element method, we numerically solved the two-dimensional Darcy equation to obtain the dynamics of a monodisperse droplet. The focus of this work was to understand the deformation of a single droplet entering a cross-shaped intersection in a confined microfluidic channel. The droplet moved through the microfluidic device to a cross-shaped intersection where the droplet experienced a hyperbolic flow. The droplet was deformed by extensional forces due to the flow rates. The deformation of the droplet in the continuous phase was characterized. The maximum deformation was rescaled in terms of capillary number, droplet size, viscosity ratio and flow rate ratio. Our numerical results for the maximum droplet deformation illustrates $\delta_{\max} \sim (1 - \exp(-b\lambda))(R/H)^{2.58}Ca^{1.01}\Lambda^{1.02}$. This numerical scaling is in good agreement with the experimental results [20].

The droplet size has a strong effect on the flow around the droplet due to the confinement (ratio of channel width to channel height), explaining the strong dependence of the droplet deformation on droplet size. Further hydrodynamic analysis including the effect of the channel thickness on the droplet deformation in our channel geometry is of interest and will be studied in a next work.

Precise information on the rheological and mechanical properties of the interface can be extracted from the study of the interface deformation under shear stress [34, 35], particularly in the presence of an adsorbed layer [19]. Direct applications are the methods employed to determine the surface tension by hydrodynamic deformation of the interface. A further motivation is the prediction of the stability of foams and emulsions, via the analysis of droplet break up conditions [36,37].

Author contribution statement

EK designed the research and developed the simulation code. AA ran the simulations. EK analyzed and interpreted the results and wrote the manuscript.

References

1. N.T. Nguyen, S. Wereley, *Fundamentals and Applications of Microfluidics* (Artech House, Boston, London, 2002).
2. S. Handayani, D.T. Chiu, E. Tjitra, J.S. Kuo, D. Lampah, E. Kenangalem, L. Renia, G. Snounou, R.N. Price, N.M. Anstey, B. Russell, J. Infect. Dis. **199**, 445 (2009).
3. G. Tomaiuolo, M. Barra, V. Preziosi, A. Cassinese, B. Rotoli, S. Guido, Lab Chip **11**, 449 (2011).
4. S. Guido, V. Preziosi, Adv. Colloid Interface Sci. **161**, 89 (2010).
5. C.N. Baroud, F. Gallaire, R. Dangla, Lab Chip **10**, 2032 (2010).
6. J.C. Baret, Lab Chip **12**, 422 (2012).
7. S. Guido, G. Tomaiuolo, C.R. Phys. **10**, 751 (2009).
8. E. Kadivar, S. Herminghaus, M. Brinkmann, J. Phys.: Condens. Matter **25**, 285102 (2013).
9. E. Kadivar, Eur. J. Mech. B/Fluids **57**, 75 (2016).
10. D.R. Link, S.L. Anna, D.A. Weitz, H.A. Stone, Phys. Rev. Lett. **92**, 054503 (2004).
11. L. Salkin, A. Schmit, L. Courbin, P. Panizza, Lab Chip **13**, 3022 (2013).
12. N. Bremond, A.R. Thiam, J. Bibette, Phys. Rev. Lett. **100**, 024501 (2008).
13. J.C. Baret, V. Taly, M. Ryckelynck, C.A. Merten, A.D. Griffiths, Med. Sci. **25**, 627 (2009).
14. E. Kadivar, EPL **106**, 24003 (2014).
15. G. Taylor, Proc. R. Soc. London, Ser. A **138**, 41 (1932).
16. G. Taylor, Proc. R. Soc. London, Ser. A **146**, 501 (1934).
17. J.M. Rallison, Annu. Rev. Fluid Mech. **16**, 45 (1984).
18. B. Bentley, L. Leal, J. Fluid Mech. **167**, 241 (1986).
19. Q. Brosseau, J. Vrignon, J.-C. Baret, Soft Matter **10**, 3066 (2014).
20. C. Ulloa, A. Ahumada, M.L. Cordero, Phys. Rev. E **89**, 033004 (2014).
21. C.D. Eggleton, K.J. Stebe, J. Colloid Interface Sci. **208**, 68 (1998).
22. H. Xi, C. Duncan, Phys. Rev. E **59**, 3022 (1999).
23. M. Nagel, F. Gallaire, Comput. Fluids **107**, 272 (2015).
24. C.A. Stan, A.K. Ellerbee, L. Guglielmini, H.A. Stone, G.M. Whitesides, Lab Chip **13**, 365 (2013).
25. C.A. Stan, L. Guglielmini, A.K. Ellerbee, D. Caviezel, H.A. Stone, G.M. Whitesides, Phys. Rev. E **84**, 036302 (2011).
26. X. Chen, C. Xue, L. Zhang, G. Hu, X. Jiang, J. Sun, Phys. Fluids **26**, 112003 (2014).
27. F. Gallaire, P. Meliga, P. Laure, C.N. Baroud, Phys. Fluids **26**, 062105 (2014).
28. K.V. McCloud, J.V. Maher, Phys. Rep. **260**, 139 (1995).
29. C. Liu, Z. Li, AIP Adv. **1**, 032108 (2011).
30. C.W. Park, M. Homsy, J. Fluid Mech. **139**, 291 (1984).
31. C. Pozrikids, *A Practical Guide to Boundary Element Methods* (CRC Press, FL, USA, 2002).
32. H.A. Stone, Annu. Rev. Fluid Mech. **26**, 65 (1994).
33. T. Cubaud, Phys. Rev. E **80**, 026307 (2009).
34. Y. Tian, R. Holt, R. Apfel, J. Colloid Interface Sci. **187**, 1 (1997).
35. J. Martin, J. Marhefka, K. Migler, S. Hudson, Adv. Mater. **23**, 426 (2011).
36. H.A. Stone, L.G. Leal, J. Fluid Mech. **220**, 161 (1990).
37. A. Ramachandran, K. Tsigklifis, A. Roy, G. Leal, J. Rheol. **56**, 45 (2012).